

Cite this: *Soft Matter*, 2014, 10, 8043

## Precision Marangoni-driven patterning†

Talha A. Arshad,<sup>ab</sup> Chae Bin Kim,<sup>a</sup> Nathan A. Prisco,<sup>a</sup> Joshua M. Katzenstein,<sup>a</sup> Dustin W. Janes,<sup>a</sup> Roger T. Bonnecaze<sup>abc</sup> and Christopher J. Ellison<sup>\*ac</sup>

A Marangoni flow is shown to occur when a polymer film possessing a spatially-defined surface energy pattern is heated above its glass transition to the liquid state. This can be harnessed to rapidly manufacture polymer films possessing prescribed height profiles. To quantify and verify this phenomenon, a model is described here which accurately predicts the formation, growth, and eventual dissipation of topographical features. The model predictions, based on numerical solutions of equations governing thin film dynamics with a Marangoni stress, are quantitatively compared to experimental measurements of thin polystyrene films containing photochemically patterned surface energy gradients. Good agreement between the model and the data is achieved at temperatures between 120 and 140 °C for a comprehensive range of heating times using reasonable physical properties as parameter inputs. For example, thickness variations that measure 102% of the starting film thickness are achieved in only 12 minutes of heating at 140 °C, values that are predicted by the model are within 6% and 3 min, respectively. The photochemical pattern that directed this flow possessed only a 0.2 dyne cm<sup>-1</sup> variation in surface tension between exposed and unexposed regions. The physical insights from the validated model suggest promising strategies to maximize the aspect ratio of the topographical features and minimize the processing time necessary to develop them.

Received 13th June 2014  
Accepted 7th August 2014

DOI: 10.1039/c4sm01284d

www.rsc.org/softmatter

## 1 Introduction

Topographically patterned coatings and substrates can enhance surface properties and enable a wide variety of important applications. Polymer films can be engineered to possess topographies that structurally mimic the lotus leaf,<sup>1</sup> to produce superhydrophobic and self-cleaning surfaces, and gecko feet,<sup>2</sup> to replicate their highly-anisotropic adhesion properties. Additionally, there are needs to create topographically patterned polymer surfaces that resist biofouling<sup>3</sup> or direct cellular alignment.<sup>4</sup> Finally, substrates and coatings with smoothly-varying thickness profiles have been employed to improve the efficiency of solar cells<sup>5</sup> and light-emitting diodes<sup>6</sup> by passively manipulating light reflections within these devices. While many applications are well-served by traditional patterning techniques such as photolithography and/or contact printing, a need exists to design new versatile and high throughput patterning methodologies that are amenable to a broader range of purposes.

To these ends, an earlier study showed that melt-state polymer flow could be photochemically directed by generating spatial surface energy patterns in glassy polystyrene (PS) films, therefore forming a topographically patterned polymer film.<sup>7</sup> The underlying mechanism for the formation of a topographic pattern is that liquids flow in response to surface tension gradients as described by the Marangoni effect.<sup>8</sup> Its physical manifestations include the “tears of wine” effect,<sup>9</sup> development of spin coating striation defects,<sup>10</sup> and surface-tension driven propulsion of floating objects.<sup>11,12</sup> A schematic for topographical patterning of polymers is shown in Fig. 1. UV irradiation through a photo-mask selectively dehydrogenates the PS backbone and increases the local surface energy in the UV exposed regions compared to the unexposed regions. This is predicted by a group contribution method and confirmed by a decrease in water contact angle. As a result, the polymer flows from low surface tension regions (unexposed to light) to high surface tension regions (exposed to light) upon subsequent thermal annealing above the glass transition temperature (*i.e.*, in the liquid state) due to the Marangoni effect. This flow creates smooth, three dimensional topography reflective of the original light exposure pattern.

However, this effort did not define any predictive capability that would enable efficient optimization of experimental variables to precisely achieve a desired topography. Theoretical models have been developed to provide this level of physical insight to other methodologies that pattern thin polymer films. Examples of such models include those developed to describe

<sup>a</sup>McKetta Department of Chemical Engineering, The University of Texas at Austin, 200 East Dean Keeton Street, Austin, Texas 78712, USA. E-mail: ellison@che.utexas.edu

<sup>b</sup>Nanomanufacturing Systems for Mobile Computing and Mobile Energy Technologies (NASCENT) Center, The University of Texas at Austin, Austin, Texas 78712, USA

<sup>c</sup>Texas Materials Institute, The University of Texas at Austin, Austin, Texas 78712, USA

† Electronic supplementary information (ESI) available: Initial concentration profile, glass transition temperature of PS, viscosity of PS blend at 120 °C, extracting surface tension and diffusivity, and secondary peaks at short thermal annealing. See DOI: 10.1039/c4sm01284d

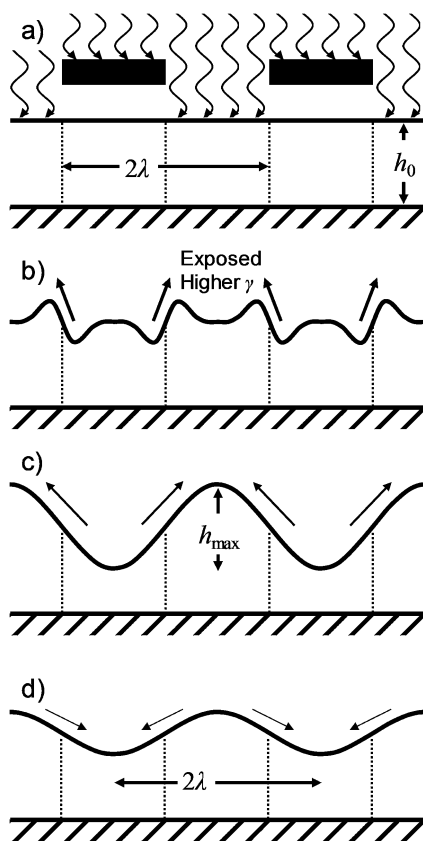


Fig. 1 Patterning schematic. (a) UV illumination through a line-and-space photo-mask possessing a half-periodicity  $\lambda$  while the polymer film is in the solid state with an initial film thickness  $h_0$ . (b) The topographical profile after a short period of thermal annealing above the glass transition temperature of the polymer shows its melt-state flow is initiated near the boundary between UV exposed and unexposed regions. (c) Further annealing develops the topographical profile into a complete sinusoidal shape with the same periodicity as the mask reaching the maximum peak-to-valley height  $h_{\max}$ . (d) The topography then dissipates after extended thermal annealing.

electrohydrodynamic patterning,<sup>13–17</sup> lithographically induced self-assembly,<sup>18–20</sup> and deformations of compliant gels by surface stresses.<sup>21–23</sup>

Here we describe a theoretical model that allows quantitative prediction of various target metrics relevant to photochemical, Marangoni-driven patterning, such as the maximum achievable feature height and annealing times necessary to achieve it. We first outline equations describing the dynamics of the film as well as the numerical method employed to solve them, their scaling and an analytical solution based on linearization. This allows comparison of model predictions, based on numerical solutions of the non-linear governing equations, with experimental observations and consideration of the role that temperature exerts on the kinetics of feature development. Finally, we identify limits on the resolution and aspect ratio the process can achieve and address the issue of how materials and experimental parameters can be judiciously selected to achieve patterns with the highest resolution or aspect ratio as efficiently as possible.

## 2 Theoretical model

### 2.1 Model and numerical method

The dynamics of the film are defined by the interplay between Marangoni and capillary forces. The photochemically induced surface tension gradient drives flow from relatively low to high surface tension regions. This is counteracted by capillary forces, which act to minimize surface area by maintaining a flat film. These dynamics are described by the thin film equation:

$$\frac{\partial h}{\partial t} + \frac{\partial}{\partial x} \left[ \left( \frac{1}{2\mu} \right) h^2 \frac{\partial \gamma}{\partial x} + \left( \frac{1}{3\mu} \right) h^3 \frac{\partial}{\partial x} \left\{ \gamma \frac{\partial^2 h}{\partial x^2} \right\} \right] = 0 \quad (1)$$

where  $h$  is the thickness of the film at any given location,  $\gamma$  is local surface tension,  $\mu$  viscosity, and  $x$  and  $t$  are the lateral distance and time, respectively.<sup>24,25</sup> The first and second terms inside the square brackets account for Marangoni and capillary flux, respectively. Van der Waals and gravitational forces are neglected since they only become relevant at length scales much smaller or larger than those of interest here. Given that the films were thin and held isothermally on a large hot plate surface during experiment, gradients in temperature across the film were not considered. The programmed surface energy is uniform parallel to the mask lines, but varies in the lateral direction perpendicular to them. Therefore, along with the thin-film condition, the equations reduce to one dimension. The local surface tension at any point is related to the concentration of the photochemically generated species which is assumed to be given by

$$\gamma = \gamma_0 + (\Delta\gamma)c \quad (2)$$

where  $c$  is the mole fraction of the photochemical product,  $\gamma_0$  is the surface tension of the original PS, and  $\Delta\gamma$  is the difference in surface tensions between neat PS and a PS with two backbone hydrogens removed per repeat unit (*i.e.* poly(phenyl acetylene)).  $\Delta\gamma$  is defined to be positive when the photoexposed polymer exceeds the base polymer in surface tension. Concentration is expressed in fractional (dimensionless) terms. The evolution of this concentration is described by:

$$\frac{\partial c}{\partial t} - \mathcal{D} \frac{\partial^2 c}{\partial x^2} + \frac{\partial}{\partial x} \left[ \left( \frac{1}{\mu} \right) h \frac{\partial \gamma}{\partial x} + \left( \frac{1}{2\mu} \right) h^2 \frac{\partial}{\partial x} \left\{ \gamma \frac{\partial^2 h}{\partial x^2} \right\} \right] c = 0 \quad (3)$$

where  $\mathcal{D}$  is the diffusivity. This is simply the convection-diffusion equation with fluid velocity being a sum of its Marangoni and capillary components (the first and second terms within the square brackets, respectively).<sup>24,25</sup> For initial periodic variations in the surface energy, the symmetry boundary conditions applied at  $x = -\lambda$  and  $+\lambda$ , where the  $x = 0$  is at the centerlines of the chrome lines on the mask under which the film is unexposed to light, are given by

$$\frac{\partial h}{\partial x} = 0 \quad (4)$$

$$\frac{\partial p}{\partial x} = \frac{\partial}{\partial x} \left( -\gamma \frac{\partial^2 h}{\partial x^2} \right) = 0 \quad (5)$$

$$\frac{\partial c}{\partial x} = 0 \quad (6)$$

A smoothed step function was employed to generate the initial concentration profile for the simulations (see Fig. S1 in ESI†). This system of non-linear equations was solved using a second-order finite difference method with explicit time stepping. Eighty node points over a half periodicity of the mask pattern are found to be sufficient for convergence.

## 2.2 Scaling & linearized solution

The relative strength of Marangoni forcing and capillary dissipation, which determine the size of the resulting peak-to-valley heights as well as the time scale over which they are formed, depend upon a number of factors: geometry (pattern periodicity and film thickness), material properties (surface tension, diffusivity and viscosity) and experimental parameters (photochemical conversion and thermal annealing temperature). To gain insight into these interrelationships, we non-dimensionalized the governing equations, employing the scales  $x \sim \lambda$  (mask half-periodicity),  $h \sim h_0$  (initial film thickness),  $c \sim c_0$  (peak fractional conversion),  $\gamma \sim \gamma_0$  (surface tension of the neat PS) and  $t \sim \mu\lambda^2/h_0\gamma_0$ . Rescaling eqn (1) and (3) to make them dimensionless but retaining the same symbols for clarity gives the following:

$$\frac{\partial h}{\partial t} + \frac{\partial}{\partial x} \left[ \left( \frac{1}{3A} \right) h^3 \frac{\partial}{\partial x} \left\{ \gamma \frac{\partial^2 h}{\partial x^2} \right\} + \left( \frac{1}{2} \right) h^2 \frac{\partial \gamma}{\partial x} \right] = 0 \quad (7)$$

$$\frac{\partial c}{\partial t} = \left( \frac{1}{P_e} \right) \frac{\partial^2 c}{\partial x^2} - \frac{\partial}{\partial x} \left[ c \left\{ \left( \frac{1}{2A} \right) h^2 \frac{\partial}{\partial x} \left\{ \gamma \frac{\partial^2 h}{\partial x^2} \right\} + h \frac{\partial \gamma}{\partial x} \right\} \right] \quad (8)$$

where  $A \equiv \lambda^2/h_0^2$  is the square of a geometric aspect ratio, and the Peclet number  $P_e \equiv h_0\gamma_0/\mu D = (\lambda^2/D)/(\mu\lambda^2/h_0\gamma_0)$  is a ratio of the diffusive timescale to the convective timescale. The third relevant dimensionless group is  $c_0\Delta\gamma$  which describes the initial surface tension difference between exposed and unexposed regions.

In order to develop analytic solutions leading to a predictive capability for feature size and time scale for feature formation for any given system, the governing equations were linearized. For small perturbations from their initial values, the film height and concentration profile are assumed to be have the forms

$$h = 1 + \eta(x, t) = 1 + \hat{\eta}(t) \frac{\cos(\pi x)}{2} \quad (9)$$

$$c = \frac{1}{2} + \xi(x, t) = \frac{1}{2} + \hat{\xi}(t) \frac{\cos(\pi x)}{2} \quad (10)$$

Here the initial concentration profile is taken to be sinusoidal:  $c_{t=0} = 0.5(1 + \cos(\pi x))$  as experimentally observed using fluorescence microscopy (see Fig. S1 in ESI†).  $\eta(x, t)$  and  $\xi(x, t)$  represent the deviation in film thickness and concentration, respectively, from their respective steady state values, 1 and 1/2.  $\hat{\eta}$  and  $\hat{\xi}$  are the purely time-dependent amplitudes of  $\eta(x, t)$  and

$\xi(x, t)$ . Substituting these into the governing equations and neglecting higher order terms, the linearized equations are then

$$\frac{\partial \hat{\eta}}{\partial t} + \left[ \left( \frac{1 + \Delta\gamma c_0 c_f}{3A} \right) \pi^4 \right] \hat{\eta} - \left[ \left( \frac{\Delta\gamma c_0}{2} \right) \pi^2 \right] \hat{\xi} = 0 \quad (11)$$

and

$$\frac{\partial \hat{\xi}}{\partial t} + \left[ \left( \frac{(1 + \Delta\gamma c_0 c_f) c_f}{2A} \right) \pi^4 \right] \hat{\eta} - \left[ \left( \Delta\gamma c_0 c_f - \frac{1}{P_e} \right) \pi^2 \right] \hat{\xi} = 0 \quad (12)$$

with the initial conditions  $\hat{\eta}(t=0) = 0$  and  $\hat{\xi}(t=0) = 1$ . These are solved to yield:

$$\hat{\eta} = \frac{\pi^2 \Delta\gamma c_0}{\psi_1 - \psi_2} \frac{2}{\psi_1 - \psi_2} (e^{\psi_1 t} - e^{\psi_2 t}) \quad (13)$$

$$\hat{\xi} = \left( \frac{\pi^4 \left( 1 + \frac{\Delta\gamma c_0}{2} \right) + \psi_1}{\psi_1 - \psi_2} \right) e^{\psi_1 t} - \left( \frac{\pi^4 \left( 1 + \frac{\Delta\gamma c_0}{2} \right) + \psi_2}{\psi_1 - \psi_2} \right) e^{\psi_2 t} \quad (14)$$

$$\text{where } \psi_1, \psi_2 = \frac{\alpha \pm \sqrt{\alpha^2 - \beta}}{2}$$

$$\text{with } \alpha = \left( 1 - \frac{\pi^2}{3A} \right) \pi^2 \frac{\Delta\gamma c_0}{2} - \pi^2 \left( \frac{1}{P_e} + \frac{\pi^2}{3A} \right) \quad (15)$$

$$\beta = \frac{\pi^6}{3A} \left( \frac{4}{P_e} - \frac{\Delta\gamma c_0}{2} \right) \left( 1 + \frac{\Delta\gamma c_0}{2} \right)$$

These describe the evolution of the film thickness and concentration profiles. The imposed surface tension profile results in the formation and growth of features when the film is thermally annealed above its glass transition temperature, which eventually decay due to capillary forces and self-diffusion.<sup>26</sup> The maximum thickness attained and the thermal annealing periods after which it is achieved can be found from:

$$\hat{\eta}_{\max} = \frac{\pi^2 \Delta\gamma c_0}{\psi_1 - \psi_2} \left\{ \exp \left[ \frac{\psi_1}{\psi_1 - \psi_2} \ln \left( \frac{\psi_2}{\psi_1} \right) \right] - \exp \left[ \frac{\psi_2}{\psi_1 - \psi_2} \ln \left( \frac{\psi_2}{\psi_1} \right) \right] \right\} \quad (16)$$

$$t(\hat{\eta}_{\max}) = \frac{\ln \left( \frac{\psi_2}{\psi_1} \right)}{\psi_1 - \psi_2} \quad (17)$$

Hence we arrive at analytical expressions for both the evolution of the film profile with time as well as the maximum feature size and associated time for any given choice of materials and experimental parameters. Eqn (16) and (17) and the appropriate scaling factors can be used to find the dimensional maximum peak-to-valley height,  $h_{\max} = \hat{\eta}_{\max} h_0$ , and the heating time necessary to achieve it,  $t_{\max} = t(\hat{\eta}_{\max}) \times \mu\lambda^2/h_0\gamma_0$ . It should be noted that since higher order terms have been ignored, these expressions apply only to situations where the non-dimensional feature size and conversion are small. However, they serve as a

useful tool to understand how the numerous independent variables and material properties affect quantities of primary interest, namely the feature size and time scale.

## 3 Experimental

### 3.1 Materials

Chemicals used in this study were purchased from Fisher Scientific or Sigma Aldrich and used as received unless otherwise noted. PS ( $M_n = 2900 \text{ g mol}^{-1}$ ,  $D = 1.2$ ) was synthesized by activators regenerated by electron transfer atom transfer radical polymerization (ARGET ATRP) and characterized as previously described.<sup>7</sup> This PS is atactic and completely amorphous exhibiting a glass transition of  $61^\circ\text{C}$  (see Fig. S2 in the ESI†). High molecular weight atactic PS ( $M_n = 50\,000 \text{ g mol}^{-1}$ ,  $D = 1.06$ ) was purchased from Pressure Chemical.

### 3.2 Sample preparation

PS (4 wt%) was dissolved in either toluene or cyclopentanone and spin coated (Specialty Coating Systems Spincoat G3-8) onto glass or silicon substrates with approximately 2 nm native oxide layers. Spin speeds varied from 1000–2000 RPM to control the film thickness. The films were stabilized against dewetting by blending 1 wt% of high molecular weight PS (50 kDa) relative to the total PS film content. The spin coated films were placed in a vacuum chamber at room temperature overnight to remove residual solvent. Thicknesses were characterized using either a Veeco Dektak 6M stylus profiler or a J.A. Woollam M-2000D Spectroscopic Ellipsometer.

### 3.3 UV exposure

In order to prescribe the surface tension pattern in the glassy PS film, the spin coated films were UV exposed using an Optical Building Blocks ScopeLite 200 through a quartz photo-mask. The typical intensity of this broadband light source at a typical exposure distance of 20 mm was measured to be  $700 \text{ mW cm}^{-2}$  using a radiometer (Fieldmax TO, Coherent, Inc.). All experiments here used a  $12.5 \mu\text{m}$  chrome line on a  $25 \mu\text{m}$  pitch photo-mask (Edmunds Optics). The light exposure dose was  $140 \text{ J cm}^{-2}$  for samples on silicon substrates and  $840 \text{ J cm}^{-2}$  for samples on glass substrates, which yield roughly the same photochemical conversion ( $\sim 6.4 \text{ mol } \%$ ) on each substrate as confirmed by Fourier transform infrared spectroscopy (FTIR) using a Thermo Nicolet 6700 FTIR with liquid nitrogen cooled MCT-B detector. These exposure doses were measured from the entire spectral output of the broadband light source (200 nm to 600 nm). Since PS absorbs only a fraction of the broadband output, significantly lower doses limited to effective wavelengths (*i.e.*  $< 300 \text{ nm}$ ), could give an equivalent result. During the UV exposure, the films were kept in the glassy state by holding the exposure stage temperature at  $20^\circ\text{C}$  using an Instec mK 1000 temperature controller. To demonstrate that dehydrogenation occurs without adverse side reactions, such as coupling and crosslinking, size exclusion chromatography and spectroscopic ellipsometry were performed showing a typical patterning light exposure procedure does not affect the

polymers' chain length distribution<sup>7</sup> or the film's glass transition temperature (see Fig. S3 in ESI†). Since the exact photochemical reaction leading to an associated surface energy gradient is unique to each polymer-light source system, the model equations were written in terms of photochemical conversion instead of light exposure dose.

### 3.4 Topography creation and characterization

After the UV exposure, the film was thermally annealed at various temperatures and annealing times to initiate the polymers' melt state flow. The annealing temperature used in experiments was confirmed by placing a type K surface thermocouple to the top surface of an uncoated substrate. The resulting topographic pattern was imaged using an optical microscope (Olympus BX 60 microscope with a Spot Insight QE camera). The evolution of topographic features at various temperatures was investigated by characterizing thickness profiles of patterned samples after sequential thermal annealing intervals. The average peak-to-valley height was determined after examining 10 half-periodicities near the center of the film.

## 4 Results and discussion

### 4.1 Physical property values

Material property values used as input for model predictions are summarized in Table 1 at the temperatures considered. The viscosity,  $\mu$ , of the PS blend as used (see *Sample preparation* in Experimental) was measured at  $120^\circ\text{C}$  under steady shear (see Fig. S4 in ESI†). This viscosity was adjusted to lower values at higher temperatures using free-volume parameters obtained from literature  $\mu(T)$  data.<sup>27</sup> A handbook value<sup>28</sup> was used for  $\gamma_0$ , the surface tension of PS, and was subsequently adjusted for smaller molecular weights and higher temperatures.<sup>29</sup>

The (dimensional) difference in surface tension between PS and poly(phenyl acetylene) (PPA),  $\gamma_0\Delta\gamma$ , was extracted from the experimentally observed feature height evolution at short times (see Fig. S5 in ESI†). While literature values for the surface energy of PPA are not available for comparison, we previously estimated using a group contribution method that  $\gamma_0\Delta\gamma$ , the difference in surface tension between PS and PPA at  $25^\circ\text{C}$ , is  $6.8 \text{ dyne cm}^{-1}$ .<sup>7</sup> Furthermore, note that an equimolar copolymer of ethylene and propylene possesses a surface tension  $1 \text{ dyne cm}^{-1}$  lower than its partially dehydrogenated form, poly(isoprene), at  $20^\circ\text{C}$ .<sup>28</sup> We consider the values of  $\gamma_0\Delta\gamma$  in Table 1 to be very reasonable because they agree in magnitude, and lie between, these examples. At the photochemical conversion typically used for patterning,  $c_0 = 6.4 \text{ mol } \%$ ,<sup>7</sup> the surface energy difference between exposed and unexposed regions,  $c_0\gamma_0\Delta\gamma$ , is at most  $0.2 \text{ dyne cm}^{-1}$ .  $c_0\gamma_0\Delta\gamma$  does not appear to have a strong temperature dependence within the relatively narrow temperature range explored in this initial work.

The effective polymer blend diffusivity,  $\mathcal{D}$ , was extracted from the feature height decay at  $120^\circ\text{C}$  observed at long experimental times (see Fig. S6 in ESI†). This value of  $\mathcal{D}$  was adjusted to higher temperatures using an Arrhenius fit to bulk self-diffusion coefficient values measured by Fleischer<sup>30</sup> for PS



Table 1 Physical property values used in model predictions

Property	Value				Ref.
	120 °C	126 °C	136 °C	140 °C	
$\mu$ [Pa s]	2550	1000	250	150	ESI <sup>27</sup>
$\gamma_0$ [dyne cm <sup>-1</sup> ]	32.2	31.7	31.1	30.8	28 and 29
$\gamma_0 \Delta \gamma$ [dyne cm <sup>-1</sup> ]	2.0	3.0	3.1	3.1	ESI
$\mathcal{D}$ [cm <sup>2</sup> s <sup>-1</sup> ]	$3.63 \times 10^{-11}$	$2.15 \times 10^{-10}$	$4.49 \times 10^{-10}$	$5.91 \times 10^{-10}$	ESI <sup>30</sup>

with  $M_W = 2.1 \text{ kg mol}^{-1}$  and  $M_W = 4.0 \text{ kg mol}^{-1}$  at temperatures between 160 °C and 220 °C to obtain the values in Table 1. Note that Ediger and coworkers<sup>31</sup> described  $\mathcal{D}(T > 84 \text{ °C})$  for a PS blend possessing  $M_W = 1.8 \text{ kg mol}^{-1}$  and  $T_g = 59 \text{ °C}$  using a WLF equation

$$\log_{10} \mathcal{D} = -14.48 + \frac{10.37(T - T_g - 16.6 \text{ °C})}{56.11 \text{ °C} + (T - T_g - 16.6 \text{ °C})}. \quad (18)$$

Our PS blend possesses  $T_g = 61 \text{ °C}$  and  $M_W = 3.98 \text{ kg mol}^{-1}$ , the latter of which is a factor 2.2 higher than that determined by Ediger and coworkers. A direct comparison can be made between their values of  $\mathcal{D}$  and the ones in Table 1 by using  $T_g = 61 \text{ °C}$  in eqn (18) and dividing the  $\mathcal{D}$  values it predicts by 2.2.<sup>32</sup> Since these values differ from ours by less than 50% at all four temperatures examined in this work, we consider the values of  $\mathcal{D}$  used in model predictions to be very reasonable. This agreement implies that this approach of extracting temperature dependent physical parameter values, such as the surface tension gradient and diffusivity, using the model with Marangoni experiments could be used to quickly characterize any polymer without sophisticated or specialized measurement methods.

## 4.2 Evolution of topographical features after annealing above $T_g$

Fig. 2 includes both experimental results and model predictions for the film thickness profile after short and long thermal annealing periods. Each different stage of topography development as illustrated in Fig. 1 is revealed by experiments and theory. It is evident that the (non-linear) model reproduces both the formation of secondary minima observed at short periods of thermal annealing and that of the complete sinusoidal features at the extended annealing periods.

Both theory and experiment reveal that the appearance of secondary peaks at short thermal annealing times is related to the shape of the initial surface tension profile. Intuitively, one expects polymer transport to occur first at the interface between exposed and unexposed regions before it can reach the regions relatively far from that interface. This concept is verified by noting that eqn (1) shows that the Marangoni flux is proportional to the second derivative of surface tension. At very short times, the film is essentially flat and capillary dissipation is negligible, resulting in maximum accumulation (and depletion) at points where the second derivative of surface tension has its

largest magnitude. At intermediate and long times, on the other hand, when capillary forces are also relevant, maxima and minima in film height coincide with the maxima and minima of the concentration profile at the centerlines of mask quartz spaces and chrome lines, respectively. When the points of maximum magnitude of the second derivative of the initial surface tension profile do not coincide with the centerlines of the mask lines and gaps, secondary peaks form at short times. As long as such a surface tension profile is present, these peaks always form; however, they may be short-lived in many cases (see Fig. S7 in ESI†). This finding is practically relevant because

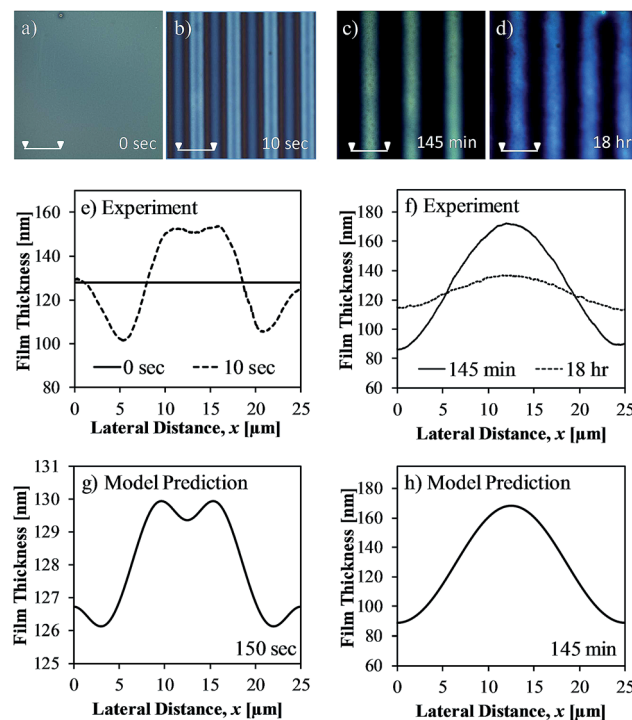


Fig. 2 Representative 100  $\mu\text{m}$  wide optical micrographs of one 128 nm thick PS film supported on a Si wafer after short (a) and (b) and long periods (c) and (d) of thermal annealing at 120 °C. Prior to the heating, the PS film was exposed to UV light through a 25  $\mu\text{m}$  pitch photo-mask. Different colors observed in the optical micrograph are light interference patterns resulting from the film thickness variations. Experimentally characterized height profiles for one periodicity from the same polymer film are shown in (e) and (f) after short and long periods of heating, respectively. Two different film thickness profiles were also theoretically predicted for a 128 nm thick film and are shown in (g) and (h), respectively.

it represents a strategy, rooted in the physical nature of fluids, to double the areal density of topographic features from that present in the projected photo-mask pattern.

It is also apt to note that the three distinct regimes of film topography evolution once heated above its glass transition temperature are strongly connected to the structure of the theoretical model. At very short times, secondary peaks form at points where the second derivative of the initial surface tension profile has its largest magnitude. At intermediate times, features rise as Marangoni flux dominates over capillary dissipation. The Marangoni driving force decays with time as polymer self-diffusion makes the concentration/surface tension profile increasingly uniform while capillary dissipation intensifies as features grow. Eventually capillary forces dominate; features begin to decay and the film tends towards its original flat form.

### 4.3 Quantitative comparison of model to experimental data

Fig. 3 depicts both the experimentally observed and non-linear model predicted evolution of peak-to-valley height,  $\hat{h}_0$ , as a function of cumulative annealing time at four different temperatures. Reasonable agreement between model predictions and experimental results are achieved for three of the four temperatures. The theoretical model quantitatively predicts both the height of features as well as the timescale associated with their growth and decay. The quality of agreement obtained at the two highest temperatures is especially encouraging since those model predictions were made with only one parameter,  $c_0\Delta\gamma$ , that was gleaned from the data itself. Unfortunately, as evident in Fig. 3, the two highest  $\hat{h}_0$  values measured at 126 °C are exceptionally large relative to the two neighboring datasets, and the model predictions do not closely match the experiments, though they both follow the same qualitative trend.

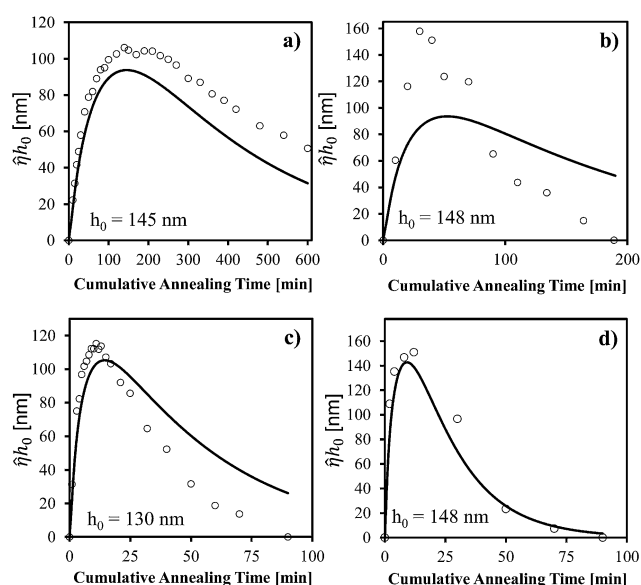


Fig. 3 Comparison of peak-to-valley height evolution between experimental results (opened circle) and model predictions (solid line) at (a) 120 °C, (b) 126 °C, (c) 136 °C, and (d) 140 °C for PS films on glass.

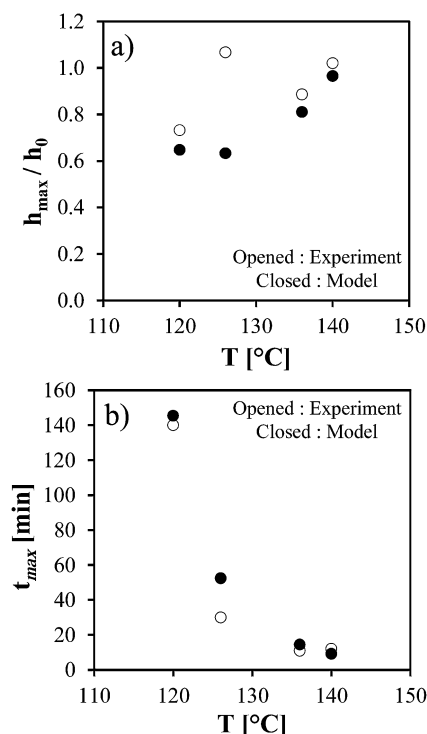


Fig. 4 (a) Attainable maximum feature size and (b) associated thermal annealing time as a function of temperature.

Raising temperature reduces the viscosity of the film and increases its diffusivity. The former promotes the formation of larger features and more rapidly, while the latter hastens the onset of decay. Any change in the patterned surface tension gradient with temperature would also affect the process. As shown in Fig. 4, higher temperatures make larger features accessible while reducing the time needed to form them. Again, only the experimental data point for  $h_{\max}$  collected at 126 °C lies outside this general trend. A 20 °C rise in temperature increases feature height by 50% while reducing the heating time eleven-fold. Higher temperatures, within material constraints, are therefore preferable as long as the films are stable.

### 4.4 Model predictions of Marangoni-driven flow at various conditions

In the context of a patterning process targeting a specific feature size, it is prudent to engineer a process wherein the maximum height attained by features coincides with the target feature height. This ensures that the desired pattern is achieved in the most efficient way possible and is an important goal to enable rapid processing methods, such as roll-to-roll processing. Therefore, key variables for the application of this technique for various purposes are the maximum feature height attained and the heating time needed to achieve it. In order to be able to design a process targeting a specific feature size with the desired resolution for a given application in the shortest possible heating time, an understanding of the limits of the process and the effects of each process variable on the two key quantities is necessary.

Fig. 5 shows how absolute feature height and thermal processing time vary as a function of the desired pattern periodicity, and how experimental parameters, namely thickness, the initial surface tension differential, and annealing temperature affect this relationship. An increase in pattern periodicity results in an enhancement in the accessible feature height but delays the achievable throughput time-scale. This is due to the fact that features farther apart can draw material from a larger region of low surface tension polymer. This effect has previously been seen in evaporative self-assembly of particles<sup>33,34</sup> where reduced pitch results in smaller features. As seen in Fig. 5, this feature height penalty worsens with decreasing periodicity whereas promotion in throughput time-scale is approximately linear on this log-log plot.

The feature height in normalized terms (*i.e.* relative to the initial film thickness) is larger for thinner films. However, the absolute height of the features above the residual layer is larger for thicker films. This means that in applications tolerant to thick residual layers, higher features can be generated by using thicker films. On the other hand, for applications in which the residual layer thickness between the feature minima and substrate surface needs to be minimized, thinner films are

preferable. The data in Fig. 5a predict that for the thinner film,  $h_0 = 145$  nm, the highest possible aspect ratio of features,  $1/2 h_{\max} \lambda^{-1}$ , is achieved for a mask with a periodicity between 10 and 25  $\mu\text{m}$ . However, for the thicker film,  $h_0 = 1000$  nm, the maximum achievable aspect ratio can be made with a mask possessing a periodicity between 100 and 200  $\mu\text{m}$ .

The initial surface tension differential is set by the UV exposure time. A longer exposure time increases the surface tension differential and results in significantly larger features. The heating time necessary to reach the maximum feature height is not strongly affected by the surface tension difference. Fig. 5c and d predict that maximizing the surface tension difference is the most effective way to manufacture films with the greatest variations in film thickness.

As noted above, higher temperature promotes the formation of larger features at faster rates. Fig. 5e and f show that while the increase in feature height resulting from a 20 degree rise in temperature to 140  $^{\circ}\text{C}$  is relatively modest ( $\sim 60\%$ ), the necessary thermal processing time shortens by well over an order of magnitude. These results for varying temperature also suggest the role the molecular weight of the polymer plays in determining feature size and heating time. Temperature affects the dynamics of the film through variation in viscosity and diffusivity. According to the Rouse model for unentangled polymer melts, the product of diffusivity and viscosity is directly proportional to temperature and inversely proportional to molecular weight.<sup>32</sup> Reduced molecular weight would therefore exert an effect on feature height and throughput time-scale as a function of pattern periodicity similar to that of increased temperature. The relatively modest rise in feature height with increased temperature is due to the fact that the viscosity of the polymer melt and the diffusivity of the photo-exposed polymers are coupled, as predicted by the Rouse model. With increasing temperature, a sharp decline in viscosity, which should promote the formation of larger features more rapidly, is accompanied by an increase in the polymers' self-diffusion, resulting in a more rapid dissipation of the surface tension gradient.

## 5 Conclusions

Here a model was introduced which accurately describes topography formation in thin polymer films which possess surface energy patterns. All of the stages of topography development (see Fig. 2) are qualitatively predicted by a relatively simple, computationally efficient adaptation of the film equation. Strictly speaking, if a polymer film possesses a surface energy pattern, even one in which the variations are only 0.2  $\text{dyne cm}^{-1}$ , Marangoni flow will result when it is heated above its glass transition. Only the size and longevity of the topographical features, which can be estimated using eqns 16 and 17, vary with the properties of the system. This, rather than a critical value of the Marangoni number, defines a criterion for feature formation.

Furthermore, the model is capable of quantitatively predicting the peak-to-valley heights of the smoothly varying thickness profile at different heating times and temperatures,

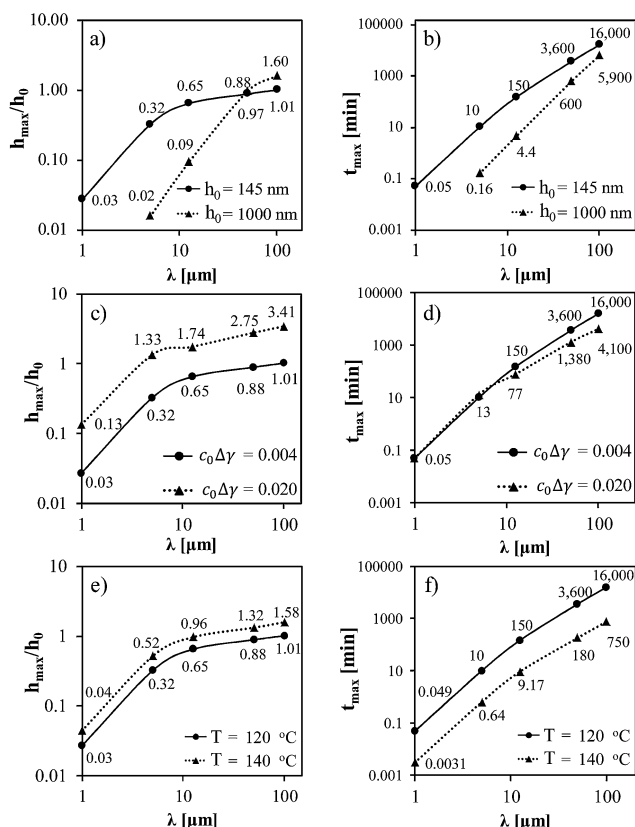


Fig. 5 Normalized maximum peak-to-valley height,  $h_{\max}/h_0$ , and heating time as a function of resolution (photo-mask half-periodicity) for different film thicknesses (a) and (b), surface tension differentials (c) and (d), and heating temperatures (e) and (f). Data points represent model predictions and lines are guides to the eye. All case studies are otherwise at identical conditions as a base condition with  $h_0 = 145$  nm,  $c_0 \Delta \gamma = 0.004$ , and/or  $T = 120$   $^{\circ}\text{C}$ .

using reasonable physical parameters as input (see Fig. 3). The model was used to define process trends to guide future development of this patterning methodology. The highest feature aspect ratios,  $1/2 h_{\max} \lambda^{-1}$ , can be achieved for thinner films, high surface energy differences between exposed and unexposed regions, a mask periodicity that is optimized for film thickness, and systems which possess both low viscosity and low self-diffusion coefficients. The formation and dissipation of film topography at excessively short and long heating times were used to extract the surface energy gradient and diffusion coefficient, respectively, at various temperatures that are reasonably well matched with literature values. Therefore, this demonstration could motivate the application of this combined theory/experimental methodology as a measurement method for surface energy changes and diffusion coefficients of any polymer in thin films, using only inexpensive bench equipment and materials.

## Acknowledgements

TAA and RTB gratefully acknowledge support from the National Science Foundation under Cooperative Agreement no. EEC-1160494. CJE, CBK, JMK, and DWJ thank the National Science Foundation CAREER Award (Grant no. DMR-1053293) for generous financial support, and Professor C. Grant Willson for allowing use of his facilities. CJE gratefully acknowledges partial financial support for this work from the Robert A. Welch Foundation (no. F-1709), 3M Nontenured Faculty Award, and the DuPont Young Professor Award.

## Notes and references

- 1 R. Dey, M. K. Raj, N. Bhandaru, R. Mukherjee and S. Chakraborty, *Soft Matter*, 2014, **10**, 3451–3462.
- 2 J. B. Puthoff, M. Holbrook, M. J. Wilkinson, K. Jin, N. S. Pesika and K. Autumn, *Soft Matter*, 2013, **9**, 4855–4863.
- 3 J. F. Schumacher, M. L. Carman, T. G. Estes, A. W. Feinberg, L. H. Wilson, M. E. Callow, J. A. Callow, J. A. Finlay and A. B. Brennan, *Biofouling*, 2007, **23**, 55–62.
- 4 H. Aubin, J. W. Nichol, C. B. Hutson, H. Bae, A. L. Sieminski, D. M. Crokek, P. Akhyari and A. Khademhosseini, *Biomaterials*, 2010, **31**, 6941–6951.
- 5 J. B. Kim, P. Kim, N. C. Pegard, S. J. Oh, C. R. Kagan, J. W. Fleischer, H. A. Stone and Y.-L. Loo, *Nat. Photon.*, 2012, **6**, 327–332.
- 6 W. H. Koo, S. M. Jeong, F. Araoka, K. Ishikawa, S. Nishimura, T. Toyooka and H. Takezoe, *Nat. Photon.*, 2010, **4**, 222–226.
- 7 J. M. Katzenstein, D. W. Janes, J. D. Cushen, N. B. Hira, D. L. McGuffin, N. A. Prisco and C. J. Ellison, *ACS Macro Lett.*, 2012, **1**, 1150–1154.
- 8 L. E. Scriven and C. V. Sternling, *Nature*, 1960, **187**, 186–188.
- 9 J. Thomson, *London Edinburgh Philos. Mag. J. Sci.*, 1855, **10**, 330–333.
- 10 D. E. Haas and D. P. Birnie III, *J. Mater. Sci.*, 2002, **37**, 2109–2116.
- 11 L. J. Burton, N. Cheng, C. Vega, J. Andrés and J. W. M. Bush, *Bioinspiration Biomimetics*, 2013, **8**, 044003.
- 12 D. Okawa, S. J. Pastine, A. Zettl and J. M. J. Fréchet, *J. Am. Chem. Soc.*, 2009, **131**, 5396–5398.
- 13 N. Wu, L. F. Pease and W. B. Russel, *Langmuir*, 2005, **21**, 12290–12302.
- 14 G. Amarandei, P. Beltrame, I. Clancy, C. O'Dwyer, A. Arshak, U. Steiner, D. Corcoran and U. Thiele, *Soft Matter*, 2012, **8**, 6333–6349.
- 15 S. A. Roberts and S. Kumar, *J. Fluid Mech.*, 2009, **631**, 255–279.
- 16 R. Verma, A. Sharma, K. Kargupta and J. Bhaumik, *Langmuir*, 2005, **21**, 3710–3721.
- 17 M. Dickey, A. Raines, E. Collister, R. Bonnecaze, S. V. Sreenivasan and C. G. Willson, *J. Mater. Sci.*, 2008, **43**, 117–122.
- 18 E. McLeod, Y. Liu and S. M. Troian, *Phys. Rev. Lett.*, 2011, **106**, 175501.
- 19 L. F. Pease III and W. B. Russel, *J. Chem. Phys.*, 2006, **125**, 184716.
- 20 E. Schäffer, S. Harkema, M. Roerdink, R. Blossey and U. Steiner, *Macromolecules*, 2003, **36**, 1645–1655.
- 21 S. Kumar, *Langmuir*, 2003, **19**, 2473–2478.
- 22 D. Paretkar, X. Xu, C.-Y. Hui and A. Jagota, *Soft Matter*, 2014, **10**, 4084–4090.
- 23 M. D. Casper, A. O. Gozen, M. D. Dickey, J. Genzer and J.-P. Maria, *Soft Matter*, 2013, **9**, 7797–7803.
- 24 O. E. Jensen and J. B. Grotberg, *J. Fluid Mech.*, 1992, **240**, 259–288.
- 25 D. P. Gaver and J. B. Grotberg, *J. Fluid Mech.*, 1990, **213**, 127–148.
- 26 D. W. Janes, J. M. Katzenstein, K. Shanmuganathan and C. J. Ellison, *J. Polym. Sci., Part B: Polym. Phys.*, 2013, **51**, 535–545.
- 27 M. L. Williams, *J. Appl. Phys.*, 1958, **29**, 1395–1398.
- 28 J. Brandrup, E. H. Immergut, E. A. Grulke, A. Abe and D. R. Bloch, *Polymer Handbook*, John Wiley & Sons, Hoboken, 4th edn, 2005.
- 29 J. Bicerano, *Prediction of Polymer Properties*, Marcel Dekker, Inc., New York, 3rd edn, 2002.
- 30 G. Fleischer, *Polym. Bull.*, 1984, **11**, 75–80.
- 31 O. Urakawa, S. F. Swallen, M. D. Ediger and E. D. von Meerwall, *Macromolecules*, 2004, **37**, 1558–1564.
- 32 P. E. Rouse, *J. Chem. Phys.*, 1953, **21**, 1272–1280.
- 33 D. J. Harris, H. Hu, J. C. Conrad and J. A. Lewis, *Phys. Rev. Lett.*, 2007, **98**.
- 34 T. A. Arshad and R. T. Bonnecaze, *Nanoscale*, 2013, **5**, 624–633.